Published in "Materials Characterization 61(6): 653-660 , 2010"
which should be cited to refer to this work.

XRCT characterisation of Ti particles inside porous Al_2O_3

S. Vasić[a,b,*], B. Grobéty[a], J. Kuebler[b,1], T. Graule[b], L. Baumgartner[c]

[a]Technical Mineralogy Group, Institute of Mineralogy and Petrography, University of Fribourg, CH-1700 Fribourg, Switzerland
[b]Empa, Swiss Federal Laboratories for Materials Testing and Research, Laboratory for High Performance Ceramics, Ueberlandstrasse 129, CH-8600 Duebendorf, Switzerland
[c]Institute of Mineralogy and Petrography, Earth Science, University of Lausanne, CH-1100 Lausanne, Switzerland

Computed X-ray tomography was used to characterise distribution and sphericity of Ti granules within highly porous (>35%) Al_2O_3 powder compacts, as they are key parameters for a successful infiltration by Fe-based alloys. Setting of reconstruction constraints, image editing as well as data processing are the most challenging parts of computed X-ray tomography and principal sources of errors that bias the generated data. Thus, corrective measures have to be applied and the reliability of generated data has to be proved with respect to statistical, stereological and volumetric aspects. Combining an adapted Interface Particle Treatment Algorithm with the Marching Cube Method, Equilibrium Random State Model, cluster splitting and conventional laser diffraction measurements a significant improvement of the three-dimensional reconstructed data was achieved. This study points out the need of the applied algorithms for the proof and improvement of generated data by computed X-ray tomography and gives a short survey of methods that can be applied.

1. Introduction

The three-dimensional (3D) characterisation and visualisation of porous powder compacts by computed X-ray tomography (CT) has nowadays become an important and powerful tool. It is an excellent technique to simultaneously obtain the amount and distribution of phase parameters for bulk materials. A straightforward use of CT is the generation of spatially resolved phase information of materials consisting of two or more phases. It allows a non-invasive, three-dimensional (3D) characterisation and visualisation of the local microstructure of porous bodies, but also the extraction of bulk properties, such as particle size distribution [1–6]. Emerging difficulties during CT generation of spatially resolved information from porous microstructures and approaches for data evaluation have been already published also in the context of metal foams [7–9]. Extensive descriptions of the CT method have been presented in many previous studies, as well as methods to emphasize the reliability of the information obtained [10–17].

Image editing as well as data processing are the most challenging parts of CT as they are the principal sources of errors. The reliability of the generated data therefore has to be proved. The most important parameters and procedures that may affect the reconstruction of the local microstructure are:

- Selection of an adequate volume element (voxel) geometry and size (e.g. the spatial resolution of the system)
- The reduction of beam hardening and ring artefacts
- The contrast and brightness thresholding of back projected images, as well as the transfer of 2D (two dimensional) information in 3D and the related potential loss of data.

For accurate extraction and reconstruction of bulk data (e.g., particle shape and particle morphology) a suitable choice

* Corresponding author. University of Fribourg, Pérolles, Ch. du Musée 6, CH-1700 Fribourg, Switzerland. Tel.: +41 78 727 70 79; fax: +41 26 300 89 36.
E-mail addresses: srdan.vasic@unifr.ch (S. Vasić), jakob.kuebler@empa.ch (J. Kuebler).
[1] Post-publication corresponding author. Tel.: +41 44 823 42 23; fax: +41 44 823 42 00.

of a voxel model is crucial [18,19]. Resolution is limited by the characteristics of the X-ray source, the geometry of the imaging system, the pixel size of the transmission images and the contrast thresholding. Objects with a magnified, projected diameter smaller than 2 pixels may not be resolved. The type and sequence of image processing procedures is often reliant on computer power. A typical image set is around 600 MB and consists of 600 individual back projected transmission images [20–22]. The first processing steps such as artefact reduction and thresholding are, therefore, performed in two dimensions (2D). Contrast and brightness thresholding of back projected 2D images is a delicate subject as the change in grey level (GL) between different phases is not sharp, but a continuous transition. Grey level values are adjusted by visual inspection of the images. If possible, thresholding should be fine tuned by comparing bulk properties, such as porosity or bulk fraction of phase extracted from the CT images, with the same properties obtained from conventional bulk characterisations [20,23,24].

However, highly porous structures (>35%) cause problems during data evaluation of back projected images as the voxels (3D pixels) of the kernel cannot be distinguished from the background which leads to large deviations of the processed phase information [19–24]. A method to avoid this problem is to demarcate a Region of Interest within the kernel that is amplified in 3D to a Volume of Interest. That in turn affects phases present at the border of the Volume of Interest in size and shape as they are cut and thus yields incorrect spatial information [15–18,22].

In this paper, the reliability of the generated information by CT to characterise porous ceramic preforms, as well as algorithms for the proof of data correctness, are discussed. Such preforms are used to produce Metal Matrix Composites (MMC) by activated pressureless melt infiltration [25–29]. Precise knowledge of the activated preform microstructure, e.g. porosity, activator concentration and even more spatial distribution is of key importance for any successful infiltration [30–34]. These parameters can be simultaneously determined by CT. The procedures, as well as methods for data verification are presented in this study.

The difficulty for the present system is the small difference in the X-ray absorption coefficients between alumina particles, air filled pores and the laboratory atmosphere. The presence of air filled pores in a highly porous sample requires the setting of a Volume of Interest (VOI), otherwise the background cannot be distinguished from the air filled pores. However, setting of a VOI influences the extracted values for particle size distribution of the activator presented by titanium (Ti). Particles, which cross the VOI boundaries are artificially cut and distort particle size distributions. An interface particle treatment (IPT) algorithm was used to increase the accuracy of CT generated data [31]. The image processing has been verified by comparing the extracted particle size distribution of titanium particles with data obtained from the starting powders using laser diffraction (LD) measurements. The comparison of CT generated particle size distribution with LD measurements as well as the introduction of an equivalent diameter for comparative purposes is investigated in previous studies [7,35]. A second check has been made to prove the spheroidicity of Ti particles by applying a surface vs. volume plot, following the Marching Cube Method [12]. This method allows the determination of spheroidicity from CT data without applying optical instruments, and identifies the spheroidicity of the 3D reconstructed Ti particles. The actual spatial distribution of the Ti particles was analysed using the Equilibrium Random State (ERS) model [36]. Assuming mono-dispersed Ti particles this algorithm indicates if activator particles are statistically in a random distribution within a VOI.

The aim of this study is the proof of the generated data with respect to statistical, stereological and volumetric aspects. Moreover the influence of the VOI setting on Ti particle size and shape, as well as on the spatial distribution, will be pointed out and opposed to data calculated by the IPT method. The necessity of this method for the determination of particle size distribution within a VOI is underlined by emphasizing the improvement of the generated data.

2. Experimental

2.1. *Materials and Instruments*

A detailed description of the preform preparation (pressed pellets: 5.5 mm high, 5 mm diameter, 65 MPa) and characterisation by LD and CT has been reported by Vasic et al. [37]. Alumina powder A100 and two different titanium powders T40 (small particles) and T200 (large particles), were added in different concentrations (i) resulting in 8 different compositions A100T40-i. (i=1, 3, 5, 10 and 20 wt.% of the alumina/titanium powder mixtures) and A100T200-i (i=3, 5 and 20 wt.%) respectively. The limiting size d for the 10% (d_{10}), 50% (d_{50}), and 90% (d_{90}) volume fractions of particles $< d$ as well as particle size distribution were determined by laser diffraction using a Malvern MasterSizerX instrument.[2] The values determined by LD served as a benchmark for the diameters determined by CT. However, LD measurements are deviated with an average error of 5% and thus cannot be taken strictly as absolute reference [5].

The principle of CT is based on the phase specific adsorption and scattering of X-ray beams and is broadly described in previous studies [10–18]. The absorption of X-rays in solids is a function of density, average atomic number and thickness of the material and is described by Beer's law (Eq. (1)):

$$I = I_0 exp(-\mu x) \quad (1)$$

where μ is the attenuation coefficient, I_0 is the initial beam intensity, and I is the measured beam intensity after it passes through the sample of thickness x [16,17]. The attenuation coefficient is very strongly dependent on the average atomic number yielding, that air and alumina can easily be discriminated against Ti. The separation of air and alumina, despite the much higher density of the latter, causes more problems as their atomic numbers do not differ significantly. However, as the presented study focuses on the extraction of Ti particles data this is not a relevant factor. A Skyscan 1072 Microtomograph[3] was used for this investigation, operated with an acceleration

[2] Malvern, Worcestershire, UK. Range: 1.2–600 μm, accuracy ≤2%.

[3] Skyscan, Kontich, Belgium.

voltage of 80 kV and a current of 120 μA. The samples were rotated through 360° and images were recorded each 0.9° with an exposure time of 5 s resulting in a total of 400 projections and a total acquisition time of 9 h. Eight frames per second were averaged for noise reduction. A 12-bit X-ray camera (CCD) couple to a scintillator served as a detector and transmission images were recorded on an area of 1024×1024 pixels. The voxel size in the back projected images is 5.5 μm/pixel. As in the present work when the X-ray source is not strictly monochromatic beam hardening occurs. Additionally, ring artefacts due to a detector non linearity may bias the reconstructed density map. These artefacts are partially taken care of by the back projecting programs and final adjustments were performed to obtain representative grey scale level for each individual phase of the sample [1,11,19].

2.2. *Image Editing*

The ConeRec routine[2] was used to perform the back projection and to reduce beam hardening and ring artefacts. The same program was used to adjust brightness and contrast on transmission images after back projection (Fig. 1a). Visual contrast and brightness adjustments were made to optimize the discrimination between the different phases by choosing constant processing conditions (e.g., thresholding for phase discrimination and splitting of particles). These adjustments had to be performed individually for each sample although the recording conditions were the same. Instrumental fluctuations and the slight differences in size and geometry between the samples are too large to allow an automated correction procedure.

A 600×600×600 voxels (=3.3×3.3×3.3 mm) volume (Volume of Interest, VOI) out of the 1024 reconstructed slices was retained for further processing. The corrected and reconstructed data represent a stack of 600 absorption maps (slices) 5.5 μm apart and 600×600 voxels in size [21,34–36]. Because of memory limitations Aphelion 3.2 software[4] (3D-reconstruction and stereological calculations), the stack was split in 5 sections, each containing 120 slices.

Aphelion 3.2 software was used to threshold the contrast of the 2D reconstructed slices and to convert the 2D slices into a 3D absorption map. Cross-checking of the known titanium contents of the individual samples was used to adjust the grey level threshold for titanium. Additionally, a convex cluster splitting was performed in order to separate aggregated particles (Fig. 1). 120 slices belonging to one section were reconstructed into a VOI of 600×600×120 voxels in size (Fig. 2).

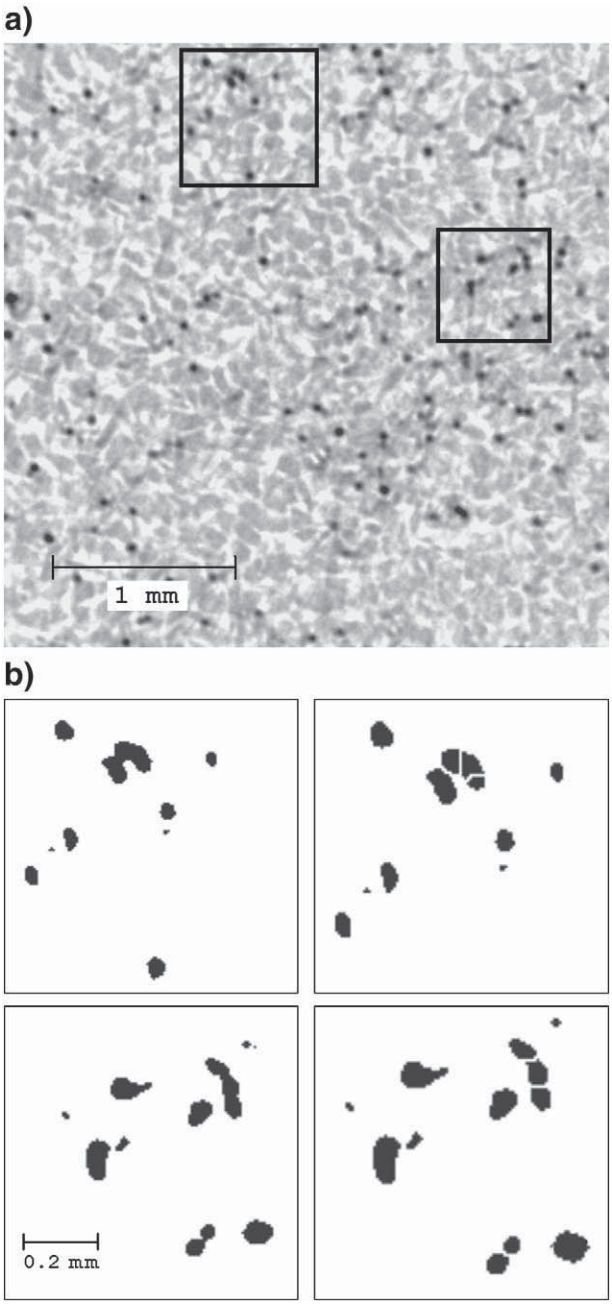

Fig. 1 – a) 600×600 large section obtained from a reconstructed slice and b) Ti particle outlines after thresholding and cluster splitting.

2.3. *Titanium Particle Data Compilation*

Position and size information of the titanium particles was extracted by a program written within the Aphelion 3.2 software shell. Data extracted are the titanium voxel coordinates and voxel counts. These parameters allow the determination of the position, centre of gravity and the equivalent sphere diameter of the particles. Each particle was also labeled. The titanium voxel counts were used to calculate the volume percentage of titanium particles relative to the VOI volume, which served as control for the reconstruction procedure. Particle size distributions were calculated by the self-written program Diameter.cls that is based on Visual Basic[5] and embedded in the Aphelion 3.2 software shell. It uses diameters of spheres with a volume that is equivalent to the volume of the counted voxels [37]. Particles cutting the VOI boundaries cause errors in the size distributions, which were corrected by a simple IPT algorithm. Particles with centre of gravity coordinates that were closer than $r_{100}=d_{100}/2$ to the VOI boundaries were skipped. Thus, the IPT treatment becomes even more

[4] Amerinex Applied Imaging, Inc., Monroe, NJ, USA.

[5] Microsoft Corporation, Redmond, WA, USA.

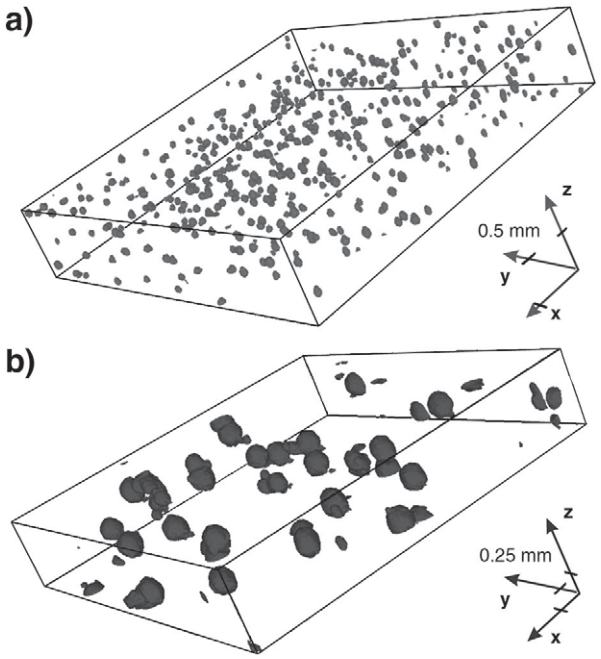

Fig. 2 – Reconstructed VOI for a) sample with T40 particles and b) with T200 particles (Aphelion 3.2).

essential when treating the data for T200 samples with the coarser titanium particles (Fig. 2). The size distribution was then reviewed again by all methods mentioned above.

2.4. *Particle Size and Shape*

The particles are close to spherical; this was already proved in a previous study by Scanning Electron Microscopy [37]. The reliability of spherically reconstructed particles from CT generated data can be tested by different methods [1,4,5,12–15]. One of them has been introduced by Helfen et al. and uses an equivalent diameter for comparison of CT and LD results [7].

In this study, the surface-to-volume ratio of the particles was used as indicator for spheroidicity [12]. The particle surface was extracted by fitting a smooth surface across the surface voxels. The fit algorithm is based on the Crofton Formula (CF) [38]. The degree of spheroidicity S is given by the ratio between the surface of a sphere with the same volume V_0 as the particle and the actual surface A_0 of the particle in (Eq. (2)):

$$S = \frac{\sqrt[3]{36\pi V^2}}{A_0} = \frac{CV_0^{2/3}}{A_0} \tag{2}$$

In a logS vs. $\log V_0^{2/3}$ plot, perfect spheres plot on a regression line with slope $(36\pi)^{1/3}$, called a compactness term, C. The average spheroidicity for any set of particles is given by the ratio of the compactness term and the actual slope. The spheroidicity is in the range between zero (0) for non spherical particles and unity (1) for perfectly spherical shaped particles (Eq. (3)). In the latter case (Eq. (2)) simplifies to (Eq. (3)):

$$A_0 = CV_0^{2/3} \tag{3}$$

Another check is the comparison of CT-derived particle size distributions with those obtained by LD measurements [5].

2.5. *Interparticle Distances and Spatial Distribution*

A homogeneous spatial distribution of the activator is important for a successful infiltration. Nearest neighbour analysis is an efficient tool to evaluate point distributions. The centre-to-centre as well as surface-to-surface interparticle distance up to the 10th nearest neighbour were determined using home-made software (programs distance.dsw, NEXT_-NAB.cls, SUR_NAB.cls) and is based on the conversion of 2D data into 3D. In order to prove the reliability of reconstructed 2D data for further data generation in 3D as well as for estimating the accuracy of image processing benchmarks, the Saltykov–Schwartz algorithm was introduced [33,39,40]. The algorithm was developed to extrapolate 3D particle size distribution as well as particle numbers per unit volume from particle contours present in 2D cross sections. It is also a valuable method for the appraisal of the procedure used for the 3D reconstruction from 2D slices [15,16]. The Saltykov method has been mainly discussed by Underwood et al., and is well suited to treating spherical particles [39,40]. The surface-to-surface distance was calculated by subtracting the sum of the equivalent sphere diameters of the particles from the centre-to-centre distance. Negative values, found during the determination of surface-to-surface distances, were interpreted as coming from particles that touched each other, and were set to zero. Negative values can also occur because the particles are not perfectly spherical. Deviations from spheroidicity are typically in the range of 0.5±0.25 pixels. The observed spatial distributions were compared with the equilibrium random state (ERS) model for mono-dispersed particles [36]. The degree of randomness in (Eq. (4)) is given by the ratio Q between ERS and experimental average nearest neighbour distances [41]

$$Q = \frac{\langle R_N^{CT} \rangle}{\langle R_N^{ERS} \rangle} \tag{4}$$

A perfectly random distribution has a ratio=1. A distribution where all points coincide (=maximal clustered) would give a ratio of 0. The maximum value is 2.25 for distributions with maximized nearest neighbour distances, e.g. for an ordered distribution of points, which corresponds to a face-centred cubic lattice [41]. Distributions of hard particles differ from point distributions by the fact that the particle centres cannot get closer to each other than the sum of the particle radii. Therefore the mean particle distance to the Nth-nearest neighbours differ significantly from the equivalent point distance. The ERS model, based on (Eq. (5)), takes into account an inhibition ratio p_N [36]:

$$p_N = \langle R_N \rangle / \langle P_N \rangle \tag{5}$$

where R_N stands for the distance to the Nth-nearest neighbours and P_N is the probability function. The average distance $<R_N>$ between a particle and its Nth-nearest neighbour corrected by the inhibition ratio is after Leggoe et al. [36] (Eq. (6)):

$$\langle R_N \rangle = \left(\frac{4}{3}\pi\lambda\right)^{-\frac{1}{3}} \cdot \left(\frac{\Gamma\left(N+\frac{1}{3}\right)}{(N-1)!}\right) \cdot \left\{1 + \left[\frac{2^{-\frac{1}{6}} \cdot (N-1)!}{\left(\frac{4}{3}\pi\lambda\right)^{-\frac{1}{3}} \cdot \Gamma\left(N+\frac{1}{3}\right)} - 1\right] \cdot \left[\frac{\Phi}{\Phi_0}\right]^{\frac{2N}{(2N+1)}}\right\} \tag{6}$$

where Γ is the Gamma function, λ are the particles per unit volume, Φ_0 is the volume of titanium particle and Φ the total volume. The ERS derived neighbour distance distributions were compared with the measured average distance distributions from CT.

3. Results and Discussion

All benchmarks used to control the success of the image processing and 3D reconstruction were positive. In a first step the titanium particle shape was roughly estimated by comparing CT reconstructed Ti within a VOI with SEM images (Figs. 2, 3). Additionally, the shape fidelity of the reconstruction procedure is underlined by the spheroidicity test for the reconstructed Ti particles. The log–log plot of volume voxels versus surface pixels for the T40 and T200 samples show a linear dependency with linear correlation coefficients very close to 1 (Fig. 4), which is expected considering the perfect spherical shape of the Ti particles as seen in SEM images. Moreover, the spheroidicity term S showed values very close to 1, and compactness C for T40 as well as T200 particles yielded good correspondence to the theoretical value of $36\pi^{1/3} \approx 4.84$.

The maxima in raw titanium particle size distributions determined by CT coincide very well with the maxima determined by LD, but the curves are shifted to lower diameters on both ends of the distribution. The discrepancy is more pronounced for the samples prepared with the T200 powder (Table 1, Fig. 5). The offset is caused by particles, which are crosscut by the VOI boundaries. Only the volume inside the VOI is considered for the calculation of the equivalent sphere diameter. The number of small particles is, therefore, increased, while the number of large particles is deficient relative to the total number of particles. After applying the IPT procedure, the differences between LD and CT-derived distribution vanishes almost completely for the T40 samples. However, The CT-derived distribution of the T200 samples still shows a slight deficiency. The larger discrepancy for the

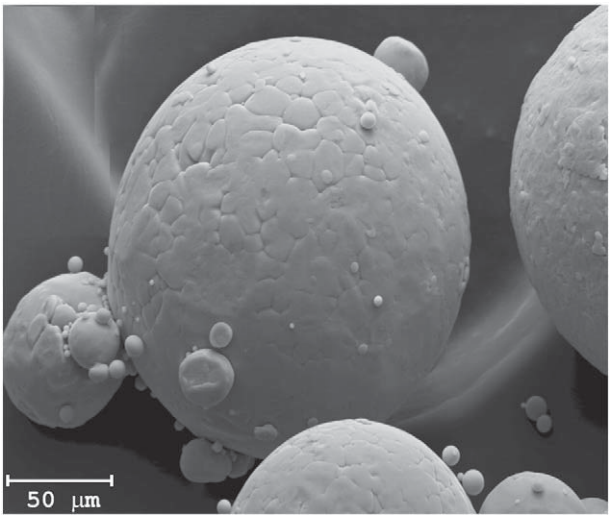

Fig. 3 – Spherical titanium particles observed by Scanning Electron Microscopy (SEM).

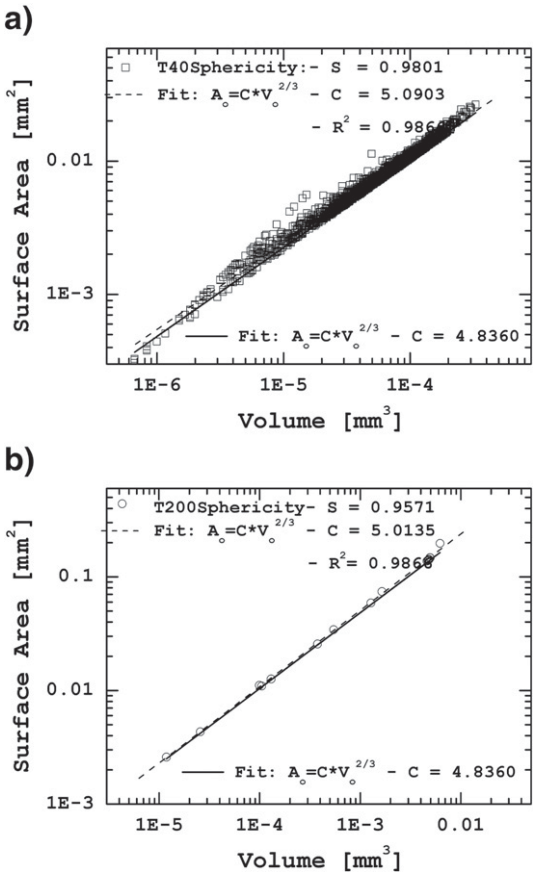

Fig. 4 – Log–log plot of surface area vs. volume$^{2/3}$ for reconstructed a) T40 and b) T200 particles. The larger spread of the data in the case of T40 particles is due to the increased clustering for the T40 particles and the related errors induced by the splitting procedure.

T200 particles can be explained by the increasing probability of large particles being located in cutting distance of a VOI wall which leads to a disproportionate exclusion of the latter and a simultaneous boost of the small particle fractions (Fig. 2). Nevertheless, characteristic diameters (d_{10}, d_{50} and d_{90}) showed very good correspondence to LD measurements after applying the IPT method (Table 1).

The 10 closest neighbour distances derived from CT reconstruction show characteristic deviations from the distances obtained from the ERS model using the same particle density (Fig. 6). All CT interparticle distances were above the

Table 1 – d_{10}, d_{50} and d_{90} values (d_{10}: 10% volume fraction; d_{50}: 50% volume fraction; d_{90}: 90% volume fraction) of T40 and T200 particles determined by LD and CT and additionally the correction with the IPT method showing a clear improvement of the values.

	T40			T200		
	d_{10} [µm]	d_{50} [µm]	d_{90} [µm]	d_{10} [µm]	d_{50} [µm]	d_{90} [µm]
LD	44	54	74	180	205	240
CT	43	57	76	145	192	204
CT-IPT	44	56	75	178	205	236

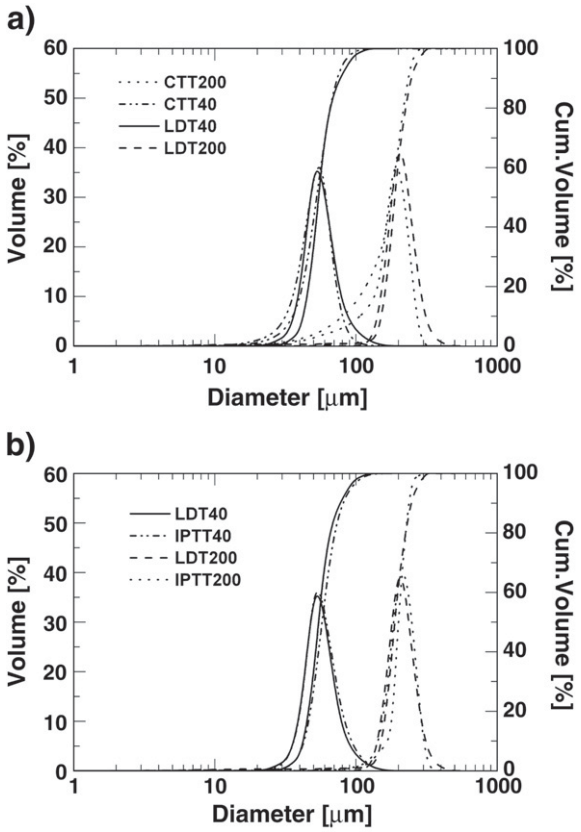

Fig. 5 – a) Particle diameter distribution for T40 and T200 particles obtained by CT and b) particle diameter distribution for T40 and T200 obtained by CT after IPT correction.

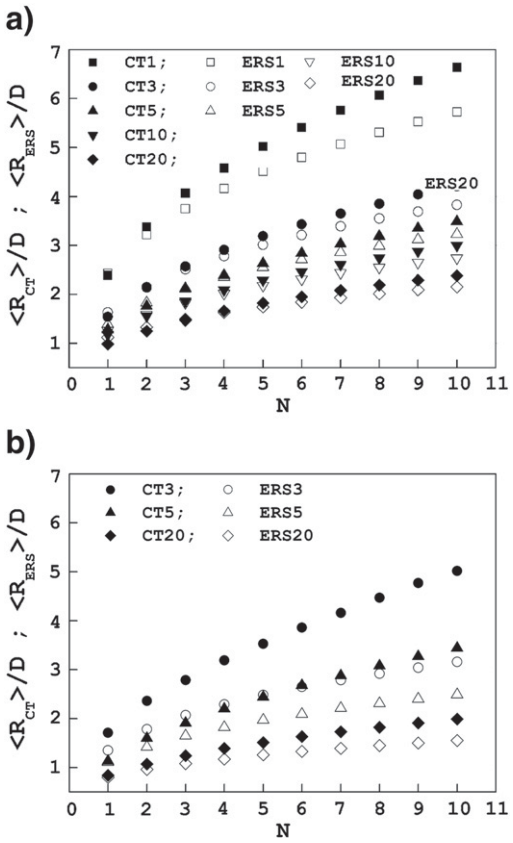

Fig. 6 – Average interparticle distance determined by CT compared to ERS for a) T40 and b) T200 particles showing deviation from random distributed state.

values determined by the ERS method as particles in reality tend to clustering and are not perfectly random distributed within a VOI.

The observed ratios Q for the nearest neighbour distances are below 1.0 for all T40 samples and decrease with increasing activator concentration, which is a clear sign of increased clustering (Table 2). T200 particles did not show significant clustering ($Q>1$) as can be seen from values in Table 3. This can be explained by the smaller number of T200 particles present within a VOI relative to T40 particles for the same activation contents. A consequence of the clustering is that the ratios increase with the order of the neighbours and becomes larger than unity. The number of neighbour distances for which the ratio is lower than unity gives an indication on the average number of particles that are present in a cluster. This number increases with increasing activator concentration and for the highest activation would be 3–4 particles, which fits quite well with direct observation of clusters. However, the process of cluster splitting was necessary, and as successfully applied as all values are close to, or even above unity.

4. Conclusions

Computed data always have to be accepted with reservation and thus correction models have to be taken into account by having in mind the influences that can affect the data. LD measurements were used as helpful benchmarks to estimate the correctness of calculated particle size distribution from CT generated data. Calculation models like the ERS, describing the evolution of Nth-nearest neighbours, successfully served for the purpose of comparison with calculated CT data. Reconstructed spheroidicity and shape fidelity of particles were checked by using the surface-to-volume/pixel to voxel ratio.

The influence on shape, size and spatial distribution of titanium cut by lateral VOI surfaces is not negligible. The correction of the data by applying the IPT method led to a significant improvement of data generated by CT with regard to particle size distribution. Distance evolution determined by CT

Table 2 – Randomness expressed by the ratio Q for T40 particles shows an increased clustering with increasing Ti content.

Ti content	1 wt.%	3 wt.%	5 wt.%	10 wt.%	20 wt.%
Nearest neighbour	Randomness Q for T40 particles				
1st	0.98	0.94	0.92	0.94	0.87
2nd	1.05	0.99	0.96	0.98	0.94
3rd	1.09	1.03	0.99	1.02	0.99
4th	1.10	1.05	1.02	1.04	1.02
5th	1.12	1.06	1.03	1.05	1.04

Note: increased clustering with increasing Ti content.

Table 3 – Randomness expressed by the ratio Q for T200 shows values above 1 and thus no significant clustering can be expected.

Randomness Q for T200 particles			
	3 wt.%	5 wt.%	20 wt.%
1st	1.27	1.02	1.05
2nd	1.33	1.13	1.11
3rd	1.35	1.16	1.15
4th	1.39	1.21	1.18
5th	1.42	1.24	1.20

was compared to the ERS method and showed characteristic deviations as particles in reality are not randomly distributed. Shape fidelity of the reconstructed particles was successfully proved by the spheroidicity test. Additionally, the clustering behaviour of the Ti particles was investigated with the characteristic ratio Q and showed an effectively performed cluster splitting.

Acknowledgement

The authors would like to thank Dr. Benita Putlitz, Susanne Skora, and Thomas Müller for the assistance and use of the X-ray microtomography equipment at the University of Lausanne.

REFERENCES

[1] Salvo L, Cloetens P, Maire E, Zabler S, Blandin JJ, Buffière JY, et al. X-ray micro-tomography an attractive characterization technique in material science. Nuclear Instrum Methods Phys Res B 2003;200:273–86.
[2] Natterer F. Numerical methods in tomography. Act Num 1999;8:107–43.
[3] Velhinho A, Sequeira PD, Martins R, Vignoles G, Fernandes FB, Botas JD, et al. X-ray tomographic imaging of Al/SiCp functionally graded composites fabricated by centrifugal casting. Nuclear Instrum Methods Phys Res B 2003;200: 295–302.
[4] Xu R, di Guida OA. Comparison of sizing small particles using different technologies. Powder Technol 2003;132: 145–53.
[5] Ma Z, Merkus HG, de Smet JGAE, Heffels C, Scarlett B. New developments in particle characterization by laser diffraction: size and shape. Powder Technol 2000;111:66–78.
[6] Farber L, Tardos G, Michaels JN. Use of X-ray tomography to study the porosity and morphology of granules. Powder Technol 2003;132:57–63.
[7] Helfen L, Baumbach T, Stanzick H, Banhart J, Elmoutaouakkil A, Cloetens P. Viewing the early stage of metal foam formation by computed tomography using synchrotron radiation. Adv Eng Mater 2002;4:808–13.
[8] Rack A, Helwig HM, Buetow A, Rueda A, Matijasevic-Lux B, Helfen L, et al. Early pore formation in aluminium foams studied by synchrotron-based microtomography and 3-D image analysis. Acta Mater 2009;57:4809–21.
[9] Watson IG, Forster MF, Lee PD, Dashwood RJ, Hamilton RW, Chirazi A. Investigation of the clustering behaviour of titanium diboride particles in aluminium. Appl Sci Manuf 2005;36:1177–87.
[10] Borbély A, Csikor FF, Zabler S, Cloetens P, Biermann H. Three-dimensional characterization of the microstructure of a metal-matrix composite by holotomography. Mater Sci Eng A 2006;367:40–50.
[11] Ketcham RA, Carlson WD. Acquisition, optimization and interpretation of X-ray computed tomographic imaginery: applications to the geosciences. Comput Geosci 2001;27: 381–400.
[12] Lin CL, Miller JD. 3D characterization and analysis of particle shape using X-ray microtomography (XMT). Powder Technol 2005;154:61–9.
[13] Masad E, Saadeh S, Al-Rousan T, Garboczi TE, Little D. Computations of particle surface characteristics using optical and X-ray CT images. Comput Mater Sci 2005;34:406–24.
[14] Maire E, Fazekas A, Salvo L, Dendievel R, Youssef S, Cloetens P, et al. X-ray tomography applied to the characterization of cellular materials: related finite element modelling problems. Compos Sci Technol 2003;63:2431–43.
[15] Proussevitch AA, Saghagian DL. Recognition and separation of dicrete objects within complex 3D voxelized structures. Comput Geosci 2001;27:441–56.
[16] Coster M, Chermant JL. Image analysis and mathematical morphology for civil engineering materials. Cem Concr Compos 2001;23:133–51.
[17] Lech M, Poledina E, Werszler A. Measurement of solid mean particle size using tomography. Powder Technol 2000;111: 186–91.
[18] Hamilton RW, Forster MF. Application of X-ray tomography to quantify the distribution of TiB_2 particulate in aluminium. Scripta Mater 2002;46:25–9.
[19] Ketcham RA. Three-dimensional textural measurements using high resolution X-ray computed tomography. J Struct Geol 2005;27:1217–28.
[20] Matejicek J, Kolman B, Dubsky J, Neufuss K, Hopkins N, Zwick J. Alternative methods for determination of composition and porosity in abradable materials. Mater Charact 2006;57:17–29.
[21] Blacher S, Leonard A, Heinrichs B, Tcherkassova N, Ferauche F, Crine M, et al. Image analysis of X-ray microtomograms of $Pd–Ag/SiO_2$ xerogel catalysts supported on Al_2O_3 foams. Colloid Surf A 2004;241:201–6.
[22] Farber L, Tardos G, Michaels JN. Use of X-ray tomography to study the porosity and morphology of granules. Powder Technol 2003;132:57–63.
[23] Taud H, Martinez-Angeles R, Parrot JF, Hernandez-Escoberdo L. Porosity estimation method by X-ray computed tomography. J Petrol Sci Eng 2005;47:209–17.
[24] Ketcham RA, Meth C, Hirsch DM, Carlson WD. Improved methods for quantitative analysis of three-dimensional porphyroblastic textures. Geosphere 2005;1:42–59.
[25] Miracle DB. Metal matrix composites — from science to technological significance. Comp Sci Technol 2005;65: 2526–40.
[26] Eustathopoulos N, Mortensen A. Capillary phenomena, interfacial bonding and reactivity. Fundamentals of Metal Matrix Composites. Stoneham: Butterworth-Heinemann; 1993. p. 42–65.
[27] Rosso M. Ceramic and metal matrix composites: routes and properties. J Mater Proc Technol 2006;175:364–75.
[28] Lemster K, Klotz UE, Fischer S, Gasser P, Kübler J. Titanium as an activator material for producing metal matrix composites (MMC) by melt infiltration. Ti-2003, 10th Proc. Conf. Titan. Hamburg: Wiley VCH; 2003. p. 2515–22.
[29] J. Kuebler, K. Lemster, P. Gasser, U.E. Klotz, T. Graule, MMCs by activated melt infiltration: High-melting alloys and oxide ceramics, presented at the 28th International Cocoa Beach Conference and Exposition on Advanced Ceramics & Composites, Cocoa Beach, 2004, unpublished.
[30] Lemster K, Graule T, Kuebler J. Processing and microstructure of metal matrix composites prepared by pressureless Ti activated infiltration using Fe-base and Ni-base alloys. Mater Sci Eng A 2005;393:229–38.

[31] Eustathopoulos N, Drevet B. Determination of the nature of metal–oxide interfacial interactions from sessile drop data. Mater Sci Eng A 1998;249:176–80.
[32] Eustathopoulos N, Nicholas MG, Drevet B. Wettability at high temperatures, vol. 3. Oxford: Pergamon Material Series; 1999. p. 106–31.
[33] Saiz E, Cannon RM, Tomsia AP. Reactive spreading: adsorption, ridging and compound formation. Acta Mater 2000;48:4449–62.
[34] Wan C, Kristalis P, Drevet B, Eustathopoulos N. Optimization of wettability and adhesion in reactive nickel-based alloys/ alumina systems by a thermodynamic approach. Mater Sci Eng A 1996;207:181–9.
[35] Erdogan ST, Gaborczi EJ, Fowler DW. Shape and size of microfine aggregates: X-ray microcomputed tomography vs. laser diffraction. Powder Technol 2007;177:53–6.
[36] Leggoe JW, Riggs JB. Nth-nearest neighbor statistics for three-dimensional equilibrium arrays of monodisperse spheres. Mater Sci Eng A 2006;426:289–97.
[37] Vasic S, Grobety B, Kuebler J, Graule T, Baumgartner L. X-ray computed micro tomography as complementary method for the characterization of activated porous ceramic preforms. J Mater Res 2007;22:1414–24.
[38] Kubinova L, Janacek J, Guilak F, Opatrny Z. Comparison of several digital and stereological methods for estimating surface area and volume of cells studied by confocal microscopy. Cytometry 1999;36:85–95.
[39] Underwood EE. Quantitative stereology. Reading, MA: Addison-Wesley; 1970. p. 75–113.
[40] Saotome A, Yoshinaka R, Osada M, Sugiyama H. Constituent material properties and clast-size distribution of volcanic breccia. Eng Geol 2002;64:1–17.
[41] Jancek J. Estimating length and surface area by systematic projections. Image Anal Stereol 2001;20:89–94.

Glossary

CT computed X-Ray tomography
3D three dimensional
2D two dimensional
MB megabyte
GL grey level
MMC metal matrix composite
VOI volume of interest
Ti titanium
IPT interface particle treatment
LD laser diffraction
ERS equilibrium random state
A100 alumina powder
T40 titanium powder (small particles)
T200 titanium powder (coarse particles)
wt.% weight percent
i titanium concentration in wt.%
d limiting diameter of particles
d_{10} 10% volume fraction of particles $< d$
d_{50} 50% volume fraction of particles $< d$
d_{90} 90% volume fraction of particles $< d$
I measured X-ray beam intensity
I_0 initial X-ray beam intensity
exp exponential function
μ attenuation coefficient
x sample thickness
CCD charge coupled device
ROI region of interest
VB Visual Basic
CF Crofton formula
S spheroidicity
V_0 particle volume
A_0 particle surface
C compactness term
Q degree of randomness
R_N^{CT} average nearest neighbour distance determined by computed X-Ray tomography
R_N^{ERS} average nearest neighbour distance determined by Equilibrium Random State model
p_N inhibition ratio
P_N probability function
R_N distance to the Nth-nearest neighbour
$\langle R_N \rangle$ average distance between a particle and its Nth nearest neighbour after Leggoe et al.
N number of particles per unit volume
Γ gamma function
λ particles per unit volume
Φ_0 volume of a particle
Φ total volume of particles